nature communications

Article

https://doi.org/10.1038/s41467-026-68824-3

Saturation of space weathering in shaping lunar regolith particle morphology

Received: 24 June 2025

Accepted: 19 January 2026

Published online: 31 January 2026

Check for updates

Ao Luo[1,6], Yifei Cui[1,6] ✉, Guodong Wang[1] ✉, Jiayan Nie[2] ✉, Chuansheng Xu[1], Zihan Zhang[1], Jun Zhang[1], Yang Li[3], Qi Zhao[4] & Huaiyu He[5]

The lunar mare regolith preserves tripartite records of volcanism, impacting, and space weathering. However, previous studies based on limited soil particle numbers were hindered by issues of sample representativeness. Here we conduct micro-CT scans of bulk soil samples from Chang'e-5 (nearside) and Chang'e-6 (farside), and develop machine learning-based image segmentation and classification methods to identify a vast number of basalt, agglutinate, breccia, and monomineralic particles. The Chang'e-5 basalt exhibits higher plagioclase content than Chang'e-6, while agglutinates from Chang'e-6 have lower void ratios, respectively indicating different lava origins and more intense micrometeorite bombardment for farside Chang'e-6. Despite their contrasting volcanic and impacting histories, the soil particles for these youngest nearside/farside samples exhibit similar morphometric distributions, suggesting that space weathering reached saturation in shaping surficial soil particle morphology in ~ 2.2 million years or less. These findings may extend to other mare regions and help establish space weathering models for other airless bodies.

The lunar mare regolith has been progressively shaped by continuous space weathering since the Moon's formation[1,2]. From the sampling efforts of the Apollo, Luna, and Chang'e missions, it is now well established that the mare regolith comprises primarily basalt, meteorite impact melt breccia, micrometeorite impact agglutinates, and monomineralic fragments[3–5]. The mineralogical and chemical compositions of mare basalts are directly linked to the nature of initial igneous magmatic processes—mantle source melting, the extent of magmatic fractional crystallization in the magma chamber, and degassing during volcanic eruption[6–10]—while their internal vesicle structures provide clues to volcanic eruption dynamics and the relative distance from source vents[11]. Following flow emplacement, the mare surface has undergone prolonged modification by meteorite impacts and solar wind irradiation[12–14]. During impacting, the lunar regolith is imparted with cumulative kinetic energy, which progressively fragments and abrades the lunar bedrock, a process referred to here as "comminution"[15]. Accompanying impacts, molten glass produced by micrometeorite collisions aggregates finer regolith particles, forming agglutinates[16]. Agglutinates are irregularly shaped and contain vesicles that not only modulate volatile escape and encode the thermomechanical conditions of micrometeorite bombardment[17], but also serve as nanoscale reservoirs capable of storing and mobilizing solar wind-derived hydrogen and water[18].

Meanwhile, fragmentation and abrasion continuously reshape particle morphologies[19,20], encoding the cumulative effects of space weathering on airless bodies[21]. On the Moon, the fraction of lunar regolith with particle sizes <1 mm is particularly relevant to surface space weathering[22] and warrants detailed investigation. Due to

[1]Department of Hydraulic Engineering, State Key Laboratory of Hydroscience and Engineering, Tsinghua University, Beijing, China. [2]School of Civil Engineering, Wuhan University, Wuhan, China. [3]Center for Lunar and Planetary Sciences, Institute of Geochemistry, Chinese Academy of Sciences, Guiyang, China. [4]Department of Civil and Environmental Engineering, The Hong Kong Polytechnic University, Hong Kong SAR, China. [5]College of Earth and Planetary Sciences, University of Chinese Academy of Sciences, Beijing, China. [6]These authors contributed equally: Ao Luo, Yifei Cui.
✉e-mail: yifeicui@mail.tsinghua.edu.cn; wgdong@mail.tsinghua.edu.cn; njiayan_@whu.edu.cn

limitations in current analytical techniques as encountered in this study, it remains challenging to obtain reliable morphometric data for particle sizes <20 μm (ref. 23), which are typically classified as "lunar dust" (see Methods). Particles within the 20–20 μm size range, comprising over 60% of the <1 mm fraction, are defined as the "bulk soil" fraction[24,25], while the remaining particles (>200 μm) are categorized as "large particles". Notably, this dominance of the bulk soil fraction is also observed in Apollo samples and can be attributed to the progressive consumption of the lunar dust fraction during agglutinate formation and its subsequent redistribution within the bulk soil fraction[22]. As such, the bulk soil fraction serves as the primary reservoir of surface evolution signatures on the Moon. The morphology of particles within this fraction not only preserves tripartite records of volcanism, impacting, and space weathering, but also exerts a critical influence on its geomechanical behavior[26]. Moreover, accurate morphological data serve as a key input for building high-fidelity predictive simulations of the Moon's surface, enabling predictive simulations of regolith behavior under various exploration scenarios[27].

On December 1, 2020, China's Chang'e-5 (CE5) mission[28] landed at 43.06°N, 51.92°W in northern Oceanus Procellarum and returned 1,731 g of regolith (Fig. 1a-b). On June 25, 2024, the Chang'e-6 (CE6) mission[24] collected 1,935.3 g of sample materials from the South Pole–Aitken basin (41.625°S, 153.978°W) via both scooping and drilling (Fig. 1a, c). These two missions provided the first paired youngest mare regolith samples (<3 Ga) from the lunar near and far sides[29,30], allowing a rare opportunity to construct a unified model of regolith evolution under comparable analytical conditions. Geochronology, geochemistry, and remote sensing data suggest that the CE5 regolith is locally derived and basaltic, with intermediate-Ti basalts[10,25], whereas CE6 soils contain a greater proportion of exotic components, including not only local basalts, mainly low- to intermediate-Ti basalts but also noritic and other components[24,31]. Silicon isotopes further reveal that the CE6 site may have undergone more intense micrometeorite bombardment than the CE5 region[32].

Despite extensive study, debate continues over the classification of basalt and the evolution of space weathering in CE5 and CE6 regolith particles. At the heart of these issues are two challenges presented by previous methods: (i) the representativeness of traditional thin-section-based geochemical analyses, which yield only two-dimensional particle data and rely on hand-picked grains; and (ii) the applicability of mineral-scale analyses and interpretations to the evolution of the whole lunar regolith in the region. In recent years, the growing accessibility of micro-computed tomography (micro-CT) has enabled its widespread application in lunar soil research[33–37]. As a non-destructive technique, micro-CT scanning allows for high-resolution reconstruction of both external particle 3D morphology and internal structures of each individual particle within the bulk soil. It enables precise quantification of the 3D morphometrics of numerous

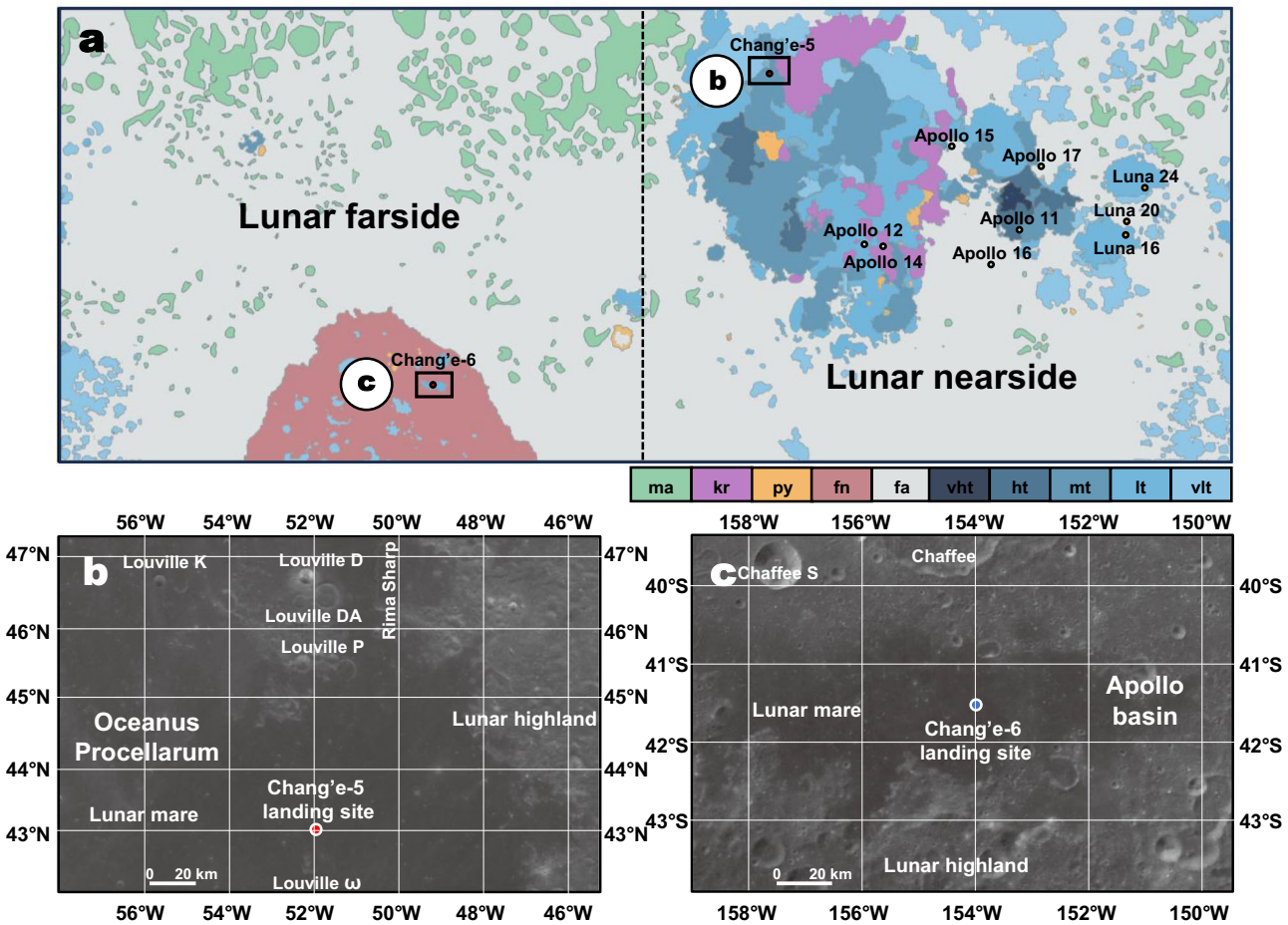

Fig. 1 | Mare regolith samples from the lunar near and far sides. a Global distribution of lunar mare regions, color-coded by Ti abundance to distinguish different mare units (vht, very high-Ti basalt; ht, high-Ti basalt; mt, medium-Ti basalt; lt, low Ti basalt; vlt, very low-Ti basalt), with major lunar endogenic lithologies[109] (ma, magnesian anorthositic suite; kr, KREEP suite; py, pyroclastic deposit; fn, ferroan noritic suite; fa, ferroan anorthositic suite). Landing sites are color-coded by mission: Apollo (green), Luna (yellow), and Chang'e (red). In **b**, **c**, CE5 and CE6 landing sites are shown on an orthographic albedo map imaged orbitally by Chang'e-2. The portion of **a** is reprinted from Science Bulletin, Volume 67, Issue 20, Chen, et al., Digital and global lithologic mapping of the Moon at a 1:2,500,000 scale, 2050-2054, Copyright (2022), with permission from Elsevier.

individual particles[23,38–40]. Recently, machine learning approaches also have also been introduced to segment large numbers of lunar regolith particles from micro-CT radiographs[23,39].

It is widely accepted that space weathering exerts a strong influence on the morphology of rock fragments on airless bodies[41–43]. However, this paradigm may not be directly applicable to the lunar surface, where particle morphology is simultaneously governed by the primary lava composition, impacting history, and the cumulative intensity of space weathering. Variations in primary lava composition give rise to distinct mineralogical assemblages in lunar regolith, which in turn affect particle-scale mechanical responses to space weathering. For instance, plagioclase is more susceptible to brittle fracture than pyroxene, rendering plagioclase-rich basalts and breccias more prone to crack formation and localized abrasion, thereby influencing particle morphology during meteoroid bombardment[15,44]. At the microscale, different mineral phases also exhibit varying responses to space weathering processes such as solar wind implantation, localized melting, and vaporization[45,46], further modifying particle morphology[47,48]. Additionally, differences in impact energy across the lunar surface produce varying degrees of lithologic fragmentation and regolith gardening effects, both of which significantly affect particle morphology[49]. Importantly, the mineralogical composition of local regolith is a key factor influencing agglutinate abundance. During rapid, non-equilibrium impact melting, low-melting-temperature mafic minerals such as ilmenite, pyroxene, and olivine are more readily incorporated into impact melts than high-melting-temperature plagioclase[50,51]. As a result, soils with higher plagioclase contents may produce fewer agglutinates[50]. The regolith maturity also exerts a strong control on agglutinate abundance, with more mature soils typically containing higher proportions of agglutinates[22]. Together, these factors influence agglutinate abundance and, consequently, the overall particle-scale morphological characteristics of regolith. Thus, the morphology of lunar regolith particles represents an integrated signature of sampling site geological and space weathering processes. Critically, the lack of comprehensive morphological data across different sampling sites has hindered the ability to disentangle these factors. To rigorously assess the morphological consequences of space weathering, assessing a vast number of particles is required, and comparative study of particle morphology across different lunar regions is urgently needed.

In this study, we apply micro-CT scans to bulk soil from the CE5 (CE5C0400YJFM01001) and CE6 (CE6C0200YJFM008) samples under identical settings, and use machine learning approaches to segment and classify individual particles in the scans. This standardized, non-destructive workflow enables high-precision quantification of 3D morphometrics and internal structures across multiple particle types. Several intrinsic limitations of micro-CT data processing are addressed in our study design. First, segmentation accuracy must be maintained across a wide range of particle sizes to ensure the fidelity of measured morphometrics. Second, the classification algorithm must operate on accurately segmented particles while retaining their internal textures, thereby enabling refined categorization and more refined interpretations of regolith formation and space weathering processes. These challenges are explicitly accounted for in our analysis. Based on this comprehensive dataset, we develop a model for the formation and evolutionary processes of the surficial mare regolith, revealing that space weathering drives morphology saturation at the particle scale across diverse particle types. Our findings provide important insights into the temporal trajectory of lunar surface modification and the convergent morphological pathways induced by prolonged space weathering.

Results

Mineralogical differences between CE5 and CE6 basalts

Based on returned mare soils[24,30] and lunar orbiter data[52], basalts represent the dominant particle type within lunar mare soils and can be used to reconstruct the thermochemical volcanic history of the Moon[7,53]. Among basaltic textures, subophitic and poikilitic types (Fig. 2a, b) are readily distinguished due to their relatively large crystal sizes and dominate the basaltic population, and can also be accurately classified using machine learning algorithms[23–25,40]. Basalt fragments, which are also prevalent (Fig. 2b), exhibit distinct striped textures that facilitate their recognition. Mineral phase densities in basalts can also be effectively distinguished through CT radiographs (Fig. 2b, c), enabling clear separation into high-density (Hp), medium-density (Mp), and low-density (Lp) phases based on grayscale intensity. Energy-dispersive X-ray spectroscopy (EDS) analyses further confirm that the Hp corresponds to ilmenite, the Mp to olivine or pyroxene, and the Lp to plagioclase (Supplementary Fig. 2f, n and o). These three phases constitute the principal mineralogical components of lunar mare basalts[30,54].

Based on analyses of 5,605 basalt particles from bulk soils (considering only intact particles, with edge-truncated particles excluded; Supplementary Video 1; Supplementary Video 2), the volume fractions of Hp, Mp, and Lp in CE5 basalts were determined as 6.80%, 53.84%, and 39.36%, respectively, and 7.16%, 61.52%, and 31.32% for CE6 (Fig. 2d). As shown in the ternary plot, the 95% probability density contour encompass all discrete basalt data points previously reported from single-particle geochemical analyses of the CE5 and CE6 samples[25,30,54]. The large dataset provided here offers an effective supplement to the more limited, discrete basaltic data derived from traditional geochemical methods applied to Apollo and Chang'e series soils. As products of continuous meteoritic impacting of a likely diverse range of cooled lava flows, basalt particles in bulk soils collectively preserve the original mineralogical signatures of lavas, enabling reliable classification of local basalt types. Notably, significant mineralogical differences are observed between CE5 and CE6 basalts, with the latter containing a lower abundance of plagioclase, which contributes to its higher density (Supplementary Fig. 4). Previous studies have suggested that both the CE5 and CE6 lavas experienced high degrees of fractional crystallization[10,31]. But the observed differences in plagioclase content may reflect varying degrees of this process between the two regions.

Traditionally, mare basalts have been classified based on major-element abundances. Electron probe microanalysis data indicate that TiO_2 and Al_2O_3 are primarily hosted in ilmenite (Hp) and plagioclase (Lp), respectively[30,54]. For large basalt particles suitable for geochemical analysis and hand-picking, linear relationships exist between ilmenite volume fraction and bulk TiO_2 content, and between plagioclase volume fraction and bulk Al_2O_3 content (Supplementary Fig. 5d, e). Applying these linear relationships, we determined bulk TiO_2 and Al_2O_3 contents of 6.08 wt% and 11.60 wt% for CE5 basalts, and 6.17 wt% and 9.43 wt% for CE6, respectively (Fig. 2e). Compared to CE6 lunar soil, CE5 exhibits considerably elevated Al concentrations, consistent with previous findings[31], thus likely categorizing CE5 mare basalts as medium-Ti and high-Al types, whereas CE6 basalts correspond to the medium-Ti and low-Al basalts, based on mare basalt classification criteria[55]. Both samples are assigned to Eratosthenian-aged mare basalts, whose TiO_2 abundances are higher than those of typical low- to medium-Ti Apollo basalts, yet lower than those of high-Ti Apollo basalts (Fig. 2e). This distinction supports the interpretation that late-stage lunar volcanism (< 3 Ga) involved distinct lava sources and evolutionary pathways from those recorded by Apollo basalts[56]. Analysis of the internal pore structures of basalts with equivalent diameters >50 μm reveals that the vast majority of void ratios in both CE5 and CE6 basalts are <2% (Supplementary Fig. 6). Such exceptionally low porosity values are characteristic of solidified, non-vesicular coherent mare basalts[11], likely formed as a result of CE5 and CE6 lavas having erupted and been emplaced at considerable distances from the source vents as flat, smooth-surfaced flows with low vesicularity, which subsequently cooled into dense basaltic units[11].

https://doi.org/10.1038/s41467-026-68824-3

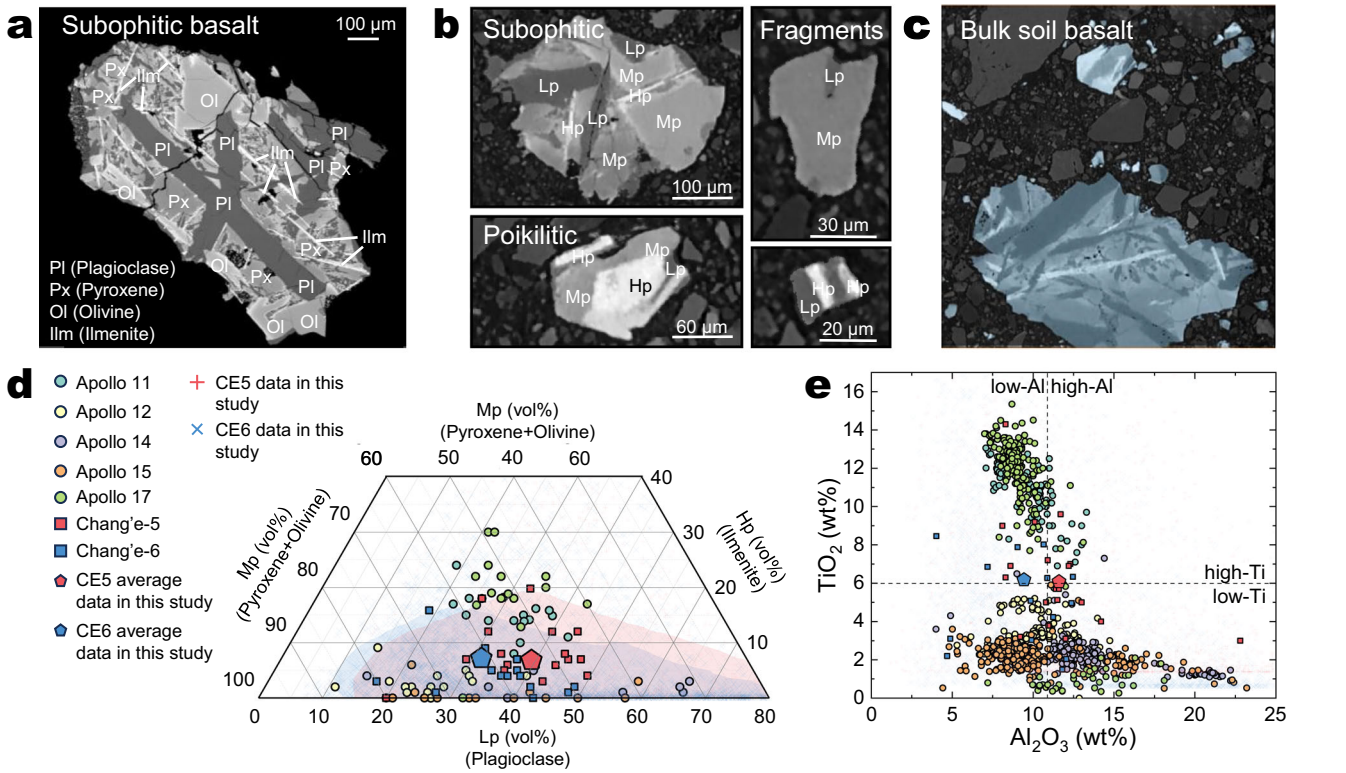

Fig. 2 | Basalt identification and mineralogical composition in CE5 and CE6 bulk soils. a Scanning electron (SE) microscopy image of a representative subophitic-textured basalt particle selected from the CE5 sample. This particle was also located within the bulk soil CT scan region and was used for intensity-density calibration in CT radiography (Supplementary Fig. 2). Labels indicate mineral abbreviations. **b** Four types of identified basalt textures. The two larger particles on the left exhibit well-preserved poikilitic and subophitic textures, which dominate the basalts composition[24,30] and are reliably classified in this study. The two smaller particles on the right display partially striped textures and are classified as basalt fragments. All basaltic particles included in this study have equivalent diameters >25 μm; particles smaller than this threshold, if assigned as basalt by machine learning, are considered potentially misclassified due to unresolved internal textures and are manually reassigned to the "unknown" group. Labels denote density-based mineral phases distinguished in CT radiographs, as defined in Supplementary Fig. 2. **c** CT radiograph of the bulk soil scan, showing basalts accurately identified using a machine learning algorithm (blue). **d** Ternary plot showing the composition of basalts in the bulk soil, classified into Hp, Mp, and Lp. Pentagons represent the average volumetric proportions of three phases in basalt from the CE5 (red) and CE6 (blue) bulk soil samples, respectively. Red and blue shaded regions represent the 95% probability density contour of the data from CE5 ($n = 2250$) and CE6 ($n = 4287$) basalts, respectively. Apollo data and individual large basalts from the CE5 and CE6 samples are also plotted for comparison[30,54,110]. **e** Average TiO_2 and Al_2O_3 compositions of basalts in bulk soil, inferred from the mineral phase proportions shown in (**d**) are based on the relationships established in Supplementary Fig. 5d, e. Pentagons and data in the background are defined in (**d**). Data from previous lunar missions are included for comparison[30,54,110].

Distinct internal vesicles of agglutinates in CE5 and CE6 soils

Agglutinates are special regolith particles consisting of smaller lunar soil fragments (mineral particles, rock clasts, and older agglutinates) bonded together by vesicular, flow-banded glass[57]. They form primarily through micrometeorite-induced melting, which generates vesiculated agglutinitic glass matrices. The vesicles within these matrices are widely interpreted as the combined textural products of solar wind implantation, which generates small vesicles along particle margins, and volatile gas exsolution during melt generation and quenching, which produces larger internal vesicles[17,57]. Within glassy matrices, submicroscopic metallic iron nanoparticles (npFe) form through a combination of micrometeorite impact[58], solar wind (induced sputtering and reduction)[59], transient thermal-spike (driven reduction)[60], and externally triggered Fe^{2+} disproportionation[61], all of which collectively modify the optical and magnetic properties of the soil. As such, agglutinates preserve detailed records of space weathering. Agglutinates occur across a wide range of particle sizes within bulk soils. Larger agglutinates (equivalent diameter >200 μm) can be easily isolated manually, whereas smaller agglutinates in bulk soil (equivalent diameter <200 μm) are typically irregular, fragile, and thus challenging to manually extract and analyze. However, this difficulty is overcome with CT scanning, as the distinctive morphological features and abundant internal porosity of agglutinates are readily identifiable in radiographs.

To further investigate agglutinate internal structure, we performed high-resolution micro-CT scans on 84 manually selected larger agglutinates (42 from CE5 and 42 from CE6). Additionally, 3D models were also acquired of numerous bulk soil agglutinates (236 from CE5 and 555 from CE6). Within the glassy regions, vesicles predominantly exhibit regular geometries (EI < 1.7, FI < 1.7, S > 0.9), whereas at the interfaces between glassy matrix and embedded fragments, vesicles become highly irregular (EI > 1.7, FI > 1.7, S < 0.9) (Fig. 3e; calculation methods for EI, FI, and S morphometrics are detailed in Methods, with illustrative examples shown in Supplementary Fig. 10). This contrast likely arises because vesicles forming within relatively homogeneous glassy regions tend to adopt regular shapes controlled by surface tension, whereas vesicles near fragment-glass interfaces are mechanically constrained by surrounding fragments and thus develop irregular morphologies. This phenomenon is also evident in SE imaging of Apollo 11 agglutinates[62]. To quantify this distinction, we define the internal regular void fraction (Ir) as the proportion of regular vesicles relative to the total vesicle count of a single agglutinate. As agglutinates are composed of both fragments and a glassy matrix[63], the glassy matrix and fragment contents (Fr) are inherently volumetrically complementary. This parameter thus may also relate to the volumetric abundance of internal fragments. To assess this possibility, we manually annotated fragments within selected larger agglutinates

https://doi.org/10.1038/s41467-026-68824-3

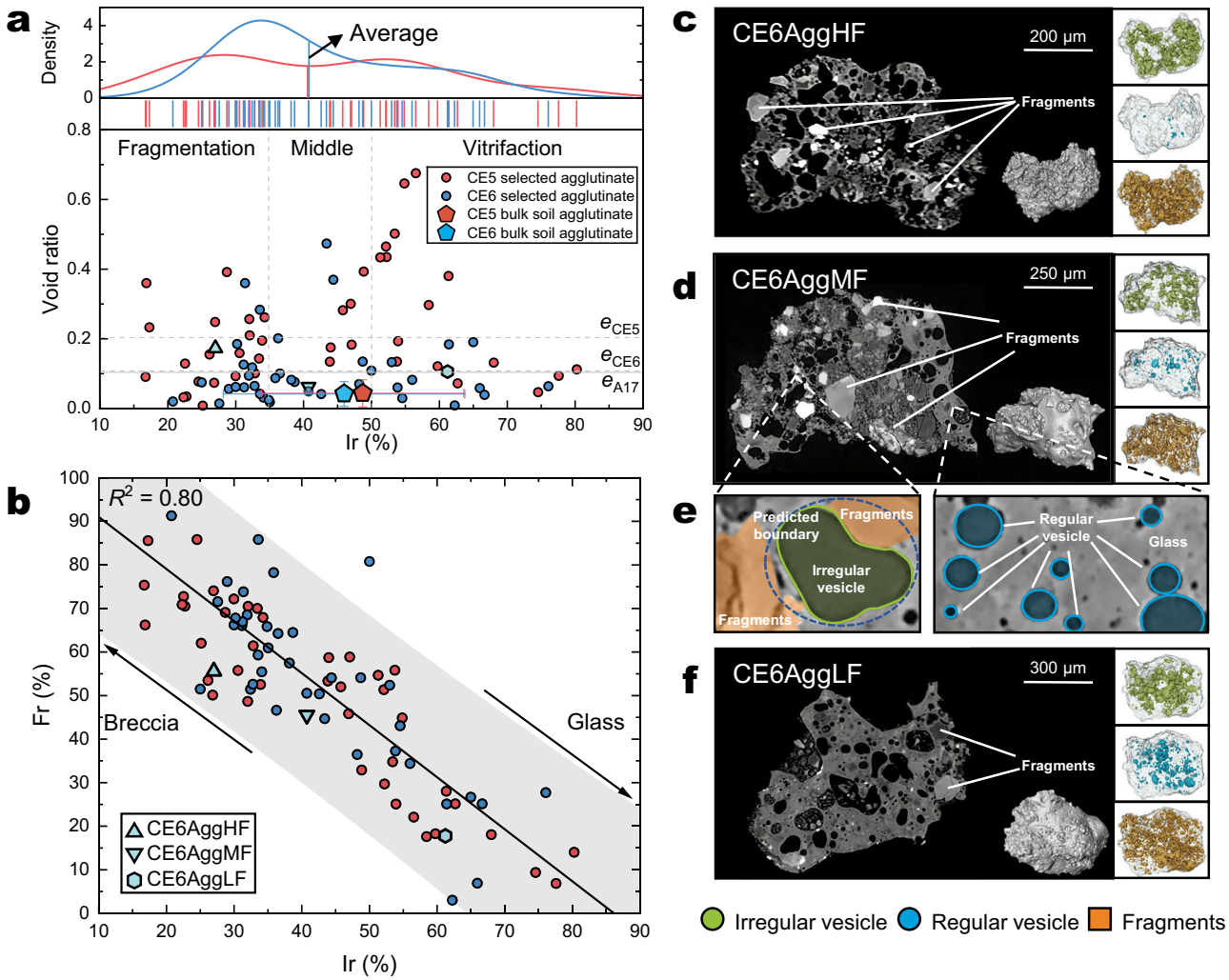

Fig. 3 | Vesicles and classification of lunar agglutinates. a Void ratios and internal regular vesicles fraction (Ir) of selected larger agglutinates from CE5 (red) and CE6 (blue) lunar samples. e_{CE5}, e_{CE6} and e_{A17} denote the average void ratios of these agglutinates, with e_{CE5} significantly higher than e_{CE6} and e_{A17}, suggesting more intense micrometeorite bombardment at the CE6 and Apollo 17 site. The average Ir values of the two groups are nearly identical, as indicated by vertical solid lines in the upper kernel density plot. Pentagons indicate average Ir and void ratios of numerous bulk soil agglutinates for CE5 (red) and CE6 (blue), with error bars representing standard deviations. The higher Ir values observed in CE5 agglutinates may be attributed to differences in internal structure. **b** Linear regression between Ir and fragment content (Fr) for selected larger agglutinates, yielding a strong inverse correlation (grey shaded region, 95% confidence interval). As Ir increases, fragment content decreases, reflecting enhanced vitrification and glass-dominant textures. Conversely, lower Ir values correspond to increased fragment content and breccia-like structures. Based on Ir values, agglutinates are classified into three types: high fragment content agglutinates, medium fragment content agglutinates, and low fragment content agglutinates. These classifications are also indicated in (**a**). In **c**, **d**, **f**, representative examples of agglutinates from each type, labeled as CE6AggHF, CE6AggMF, and CE6AggLF, are marked with light blue symbols in (**a**, **b**). The left panels show the CT radiographs, while the right panels present 3D reconstructions of internal structures: irregular vesicles (red), regular vesicles (blue), and fragments (yellow). These visualizations confirm the statistical trends observed in (**b**). **e** Enlarged view of vesicles within agglutinates, illustrating that vesicles formed adjacent to fragments are more irregular due to mechanical constraint, while vesicles developed within the glassy matrix are more regular.

(Supplementary Fig. 8a, d), finding a strong inverse correlation between Ir and Fr (Fig. 3b). Based on Ir values, we categorize agglutinates into three classes: (i) those with Ir <0.35 are fragmentation-defined as high fragment content agglutinates (Fig. 3c), (ii) those with Ir >0.5 are vitrifaction-defined as low fragment content agglutinates (Fig. 3f), and (iii) those with intermediate Ir values (0.35–0.5) are classified as medium fragment-content agglutinates (Fig. 3d). For the broader population of bulk soil agglutinates, Ir was directly used as a proxy to estimate internal fragment abundance.

Our results show no significant differences in the distribution or mean Ir values between the larger agglutinates of CE5 and CE6, where $Ir_{CE5} \approx Ir_{CE6} = 0.42$ (Fig. 3a). However, internal porosity measurements consistently show a considerable lower average void ratio in CE6 agglutinates ($e_{CE6} = 0.11$) compared to those from CE5 ($e_{CE5} = 0.23$) (Fig. 3a). For agglutinates in bulk soils, Ir values are higher in CE5 (Ir = 0.49) than in CE6 (Ir = 0.46). Compared to their larger counterparts, the bulk soil agglutinates from CE5 exhibit a modest increase in Ir values, suggesting a relatively lower internal fragment content (Fig. 3a). Given that bulk soil agglutinates likely represent the fragmented products of larger agglutinates[64], this trend may reflect inherent structural differences in the initial agglutinates of the two regions, which could in turn influence their subsequent response to space weathering.

Morphological homogenization among similar lunar regolith particle types

The morphology of lunar regolith particles records long-term space weathering processes on the lunar surface[23]. Using machine learning

segmentation and classification methods, we obtain morphometrics—aspect ratio, sphericity, convexity, and roundness—with definitions provided in the Methods and Supplementary Fig. 10, for no fewer than 100 individual effective and intact particles from each particle category from both CE5 and CE6 bulk soil CT scans, ensuring statistically representative datasets for each particle type. The analyzed particle types include basalts, agglutinates, breccias, high-density (Hm), medium-density (Mm), and low-density (Lm) monomineralic particles, as well as glass beads (Fig. 4a). The Hm, Mm, and Lm groups are readily distinguishable in radiographs based on their X-ray attenuation intensities, where Hm is primarily composed of the opaque Fe-oxide mineral ilmenite, Mm mainly represented by pyroxene, olivine, or anisotropic glass, and Lm consists predominantly of plagioclase grains[23,65]. Breccias were also included; however, due to their limited abundance, their morphometric distributions may not be statistically robust. Glass beads were omitted, given their highly regular, nearly spherical shapes, with morphometrics closely approximating those of ideal spheres (Fig. 4a). To examine potential size-dependent effects, Mm and Lm particles were subdivided into larger (equivalent diameter >50 μm) and smaller (equivalent diameter <50 μm) fractions. Our results show that aspect ratio is virtually unaffected by particle size, while sphericity and convexity exhibit only minor size dependence. In contrast, roundness is strongly influenced by particle size, with smaller particles being rounder (Fig. 4c). This trend likely reflects the scale-dependent nature of morphological descriptors and is consistent with observations from Apollo lunar soil studies[37].

Our morphology results also indicate remarkable consistency across the distributions of all morphometrics for basalt, breccia, agglutinate, Hm, Mm (both size fractions), and Lm (both size fractions) particles from CE5 and CE6 soils (Fig. 4b, c). Differences in mean morphometrics for corresponding particle categories between the two sites are all within 5% (Supplementary Table 3). The overall regularity (OR) of different particle types exhibits two distinct regimes. More than half of the basalt and monomineralic particles (Hm, Mm, and Lm), in terms of particle number, fall within an OR range of 0.63–0.75 (Fig. 4d). These particle types represent the majority of the bulk soil population (>60 vol%). These particles, characterized by simple internal structure, are herein referred to as "simple particles." In contrast, breccia and agglutinates display considerably lower OR values than other particle types, indicating a markedly more irregular morphology (Fig. 4d). Owing to their complex internal structure, these particles are categorized as "complex particles." Using the same methods applied to the lunar regolith, we additionally analyzed the morphometric distributions of a large number of particles from the lunar regolith simulant (LRS: IGG-01), which was produced by mechanically crushing basalt[66]. Compared to lunar basalt particles, the LRS particles exhibit lower aspect ratios (Fig. 4b). Such characteristics are consistent with the angular-to-subrounded morphologies observed on asteroid regolith surfaces, where particles typically experience short surface residence times and limited abrasion[67,68]. This similarity likely reflects the fact that both mechanically crushed simulants and asteroid regolith are dominated by relatively "fresh" fragments that have not undergone prolonged regolith gardening.

Building on particle classification, we quantified the relative abundances of each particle type (Fig. 4e). In particular, agglutinate abundance can serve as an indicator of soil maturity[57]. This parameter correlates positively with the maturity index Is/FeO, but only when Is/FeO <60, above which agglutinate abundance is known to saturate in highly mature soils[69,70]. The CE5 bulk soil exhibits an Is/FeO value of ~14, consistent with immature soils[71], and an agglutinate abundance of ~8%. In contrast, CE6 soils yield an Is/FeO value of ~56.5, characteristic of mature soils[72], together with a higher agglutinate abundance of ~17%. The elevated agglutinate abundance and Is/FeO value of CE6 are consistent with trends established in previous studies[70]. Furthermore, the Is/FeO index is closely linked to the abundance of npFe, produced on grain rims and within agglutinates by micrometeorite bombardment and solar wind sputtering/redeposition, and therefore reflects the cumulative intensity of these space weathering processes. Another critical component of space weathering is regolith "gardening" driven by meteorite impacts, which is commonly expressed through the surface soil maximum exposure age, where soils with longer exposure durations experience more extensive overturn and reworking[73]. According to regolith evolution models, CE5 surface soils have a maximum exposure age of ~2.2 Ma, whereas CE6 soils have been exposed since ~3.2 Ma (ref. 74). The slightly longer exposure duration of CE6 regolith suggests a greater degree of surface soil gardening, and together with these maturity indices, consistently demonstrates that CE6 soils have experienced a higher overall degree of space weathering.

Discussion

The CE5 and CE6 lunar missions have provided an opportunity to perform a comparative analysis of lunar regolith from both the near and far sides of the Moon. Using high-resolution micro-CT scans, we non-destructively obtained the morphology, internal structure, and 3D distribution of mineral phases for diverse types of lunar regolith particles. This method enables efficient bulk analysis of the mare regolith composition at the sampling sites and allows us to investigate its formation and evolutionary processes. The mare regolith is primarily composed of weathering products from the basalt layer beneath the surface regolith, which itself was formed by modification of the cooled mare lava[75,76] (Fig. 5). Over time, continuous impact "gardening" has thoroughly mixed the various basalts within the regolith, resulting in a fairly homogeneous distribution of basalt particles[77].

Our analyses reveal both similarities and some striking differences between CE5 and CE6 mare basalts in terms of bulk chemical composition and major mineral abundances. Both Chang'e regolith samples display distinctly elevated titanium (Ti) and aluminum (Al) abundances. Moreover, the younger CE5 basalt exhibits an even higher Al content than CE6 (Fig. 2e), consistent with analyses performed on large basalt fragments from these sites[53]. This chemical signature likely indicates a common petrogenetic process for younger mare basalts (<2.8 Ga) that differs fundamentally from those responsible for older mare basalts (>3.15 Ga). Such an interpretation is further supported by independent studies reconstructing basalt formation mechanisms based on pyroxene composition analyses from both Apollo samples and the younger Chang'e basalts[78]. Interestingly, the relationships between basalt and bulk soil grain-specific gravity between the two landing sites appear to be inverted (Supplementary Fig. 4). While the CE5 basalts exhibit a lower density due to their higher plagioclase content, bulk mineralogical analyses of the CE6 regolith suggest a higher plagioclase abundance[24], implying a lower bulk soil density at that site. Previous investigations have shown that the CE5 regolith is primarily derived from the in-situ weathering of mare basalts[43]. In contrast, the bulk characteristics of the CE6 regolith may indicate substantial mixing with non-mare materials enriched in plagioclase (Fig. 5). This hypothesis has been corroborated by geochemical analyses of a large number of individual regolith particles, which reveal the incorporation of noritic components likely sourced from the Apollo basin into the CE6 landing site deposits[79].

Agglutinates, abundantly distributed throughout lunar soils, serve as critical indicators of micrometeorite impact histories[80]. Based on existing theoretical models, given the absence of hemispheric asymmetry in micrometeorite flux at the lunar surface[81] and the nearly identical absolute latitudes of the CE5 and CE6 sampling sites, the micrometeorite fluxes at the two regions are expected to be highly similar[81,82]. Therefore, the notably distinct internal structures observed between CE5 and CE6 agglutinates likely reflect regionally different micrometeorite bombardment intensities. The comparatively lower internal porosity observed in larger CE6 agglutinates is consistent with

https://doi.org/10.1038/s41467-026-68824-3

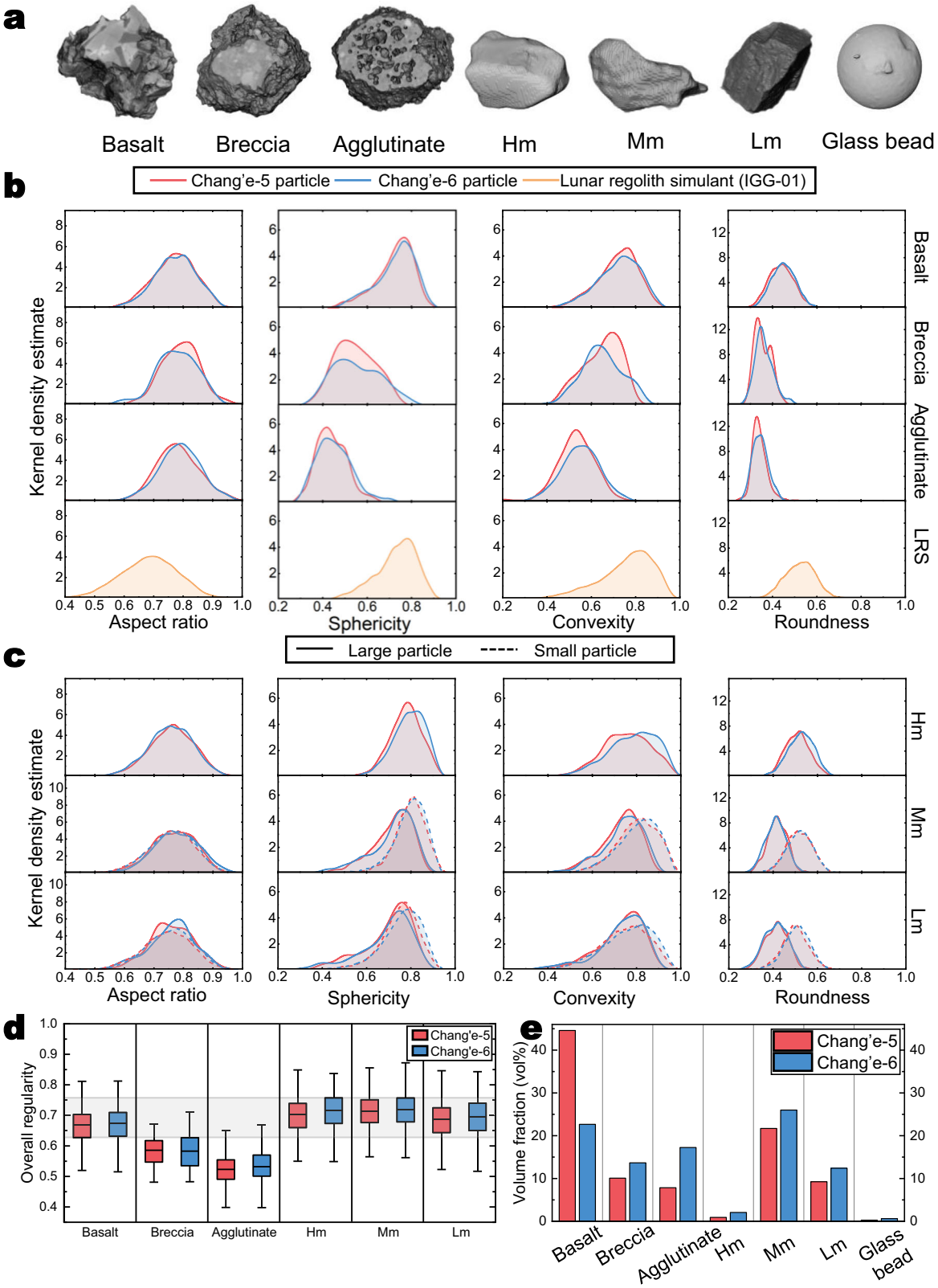

more efficient volatile gas escape under open-system conditions. Micrometeorites with higher impact velocities and larger masses generate higher transient temperatures[32], which lower melt viscosity and promote rapid bubble ascent and vesicle coalescence, thereby facilitating volatile gas venting before cooling[83–85] (Fig. 5). Experimental simulations have also demonstrated that higher molten glass temperatures facilitate more rapid volatile gas escape from forming agglutinates[17]. Consequently, the reduced porosity of CE6 farside samples points toward more intense micrometeorite bombardment, generating higher molten glass temperatures at this landing site. Previous research has shown that CE5 samples experienced relatively lower temperatures (1200–2000 K, ref. 32) induced by micrometeorite impacts compared to Apollo soil samples[86], although such temperatures are already sufficient to melt regolith and generate agglutinates.

Fig. 4 | Morphometrics of diverse particle types in CE5 and CE6 soils. **a** Representative 3D morphologies of each of the seven lunar regolith particle types—basalt, breccia, agglutinate, Hm, Mm, Lm, and glass beads—identified via our machine learning approach of lunar bulk soil. **b** Morphometrics statistical distributions for rock particles (basalt, breccia, and agglutinate) in bulk soil and LRS (IGG-01). **c** Morphometrics statistical distributions for monomineralic particles (Hm, Mm, and Lm) in bulk soil. Size-dependent effects on morphometrics were specifically investigated for Mm and Lm particles by subdividing them into large (solid lines) and small (dashed lines) size groups. Comparisons between nearside and farside samples reveal highly similar mean values, standard deviations, and distribution ranges across all particle types. **d** Boxplots comparing the overall regularity (OR) of six particle types in nearside and farside bulk soils. Black lines indicate medians; boxes represent the lower and upper quartiles; whiskers denote the full range of the distributions. The shaded region highlights the concentration OR range for "simple particles." Agglutinate and breccia particles show considerably lower OR values compared to other particle types. In general, the OR distributions for CE5 and CE6 are very similar, with slightly more regular particle shapes observed in the CE6 regolith. **e** Volume fractions of each particle type in the CE5 and CE6 regolith bulk soil samples were determined in this study. Owing to a higher degree of space weathering at the CE6 landing site, it contains approximately ~9% more agglutinates and ~4% more breccia than the CE5 regolith.

For CE6 samples, the discovery of oldhamite[87] and silicon isotope modeling suggests that the glass formation temperatures are likely comparable to those documented in Apollo samples, including Apollo 17 (2500–5000 K, ref. 32,86). To further evaluate this hypothesis, we extracted the 3D morphologies of 42 agglutinates from radiographs of Apollo 17 sample 73002 (ref. 88). These particles exhibit an average void ratio of 0.10, closely matching that of CE6 larger agglutinates (Fig. 3a), thereby providing additional support for our interpretation. An alternative explanation for the higher porosity observed in CE5 agglutinates is that CE5 regolith contains a higher proportion of mafic components[24,25], leading to lower melting temperatures and extremely rapid cooling of agglutinitic melts, which may trap more volatile gas within the agglutinate interiors. However, we emphasize that final porosity also depends on melt viscosity, cooling and welding history, vesicle connectivity, and possible post-formation collapse, so this interpretation should be regarded as plausible rather than unique.

In parallel, differences in volatile content may also contribute to the divergence in agglutinate void ratios. Recent studies have detected the presence of water in CE5 soils[89], and the extended impacting history at the CE6 site raises the question of whether repeated melting and resolidification events may influence gas escape efficiency, which is an issue that warrants further investigation. Taken together, the observed differences in porosity of larger agglutinates at the two landing sites likely contribute to the slight variation in Ir values measured in bulk soil agglutinates. The relatively lower porosity of CE6 agglutinates suggests a higher proportion of glass content. Accordingly, CE5 agglutinates tend to exhibit honeycomb-like structures with elevated porosity (Supplementary Fig. 8a, b), whereas those from CE6 contain smaller vesicles and lower porosity (Supplementary Fig. 8d, e). In the case of CE5, space weathering processes (mainly "gardening" processes), including successive abrasion and fragmentation, act on agglutinates with higher porosity and larger vesicles, where internal fragments are bound by relatively fewer glassy matrix connections. Under prolonged regolith gardening, shear stresses acting on such structures can promote particle fragmentation, leading to the preferential loss of fragment-bearing regions (Supplementary Fig. 8b, c). At the bulk soil scale, this process reduces the abundance of internal fragments, exposes or removes irregular vesicles, and leaves behind agglutinates dominated by regular vesicles formed within the glassy matrix, thereby producing higher Ir values (Fig. 3a). In contrast, CE6 larger agglutinates contain more densely packed fragments embedded within glassy matrix, and their evolution is governed primarily by abrasion (Supplementary Fig. 8e, f). These more strongly welded structures are more resistant to fragment loss, which may help preserve internal fragments in bulk soil agglutinates and result in slightly lower Ir values compared with CE5 bulk soil agglutinates.

Particle reshaping processes at the lunar surface include impact gardening (mainly abrasion caused by interactions among large numbers of particles within a given region[80]), impact fragmentation (grain breakage due to direct energy deposition during impacts[90]), impact agglutination (where impact-induced melts or semi-plastic phases fuse surrounding grains into agglutinates and breccias), impact sputtering (deposits from impact events appear randomly on the surface of minerals, forming sputtering deposit layer that modify particle morphology[46]), impact abrasion (localized surface wear induced by micrometeoroid impacts[20,91] or secondary impacts that generate linear scratches[92]), thermal fatigue (fracturing driven by thermal stresses leading to ultimate grain disintegration[88]), and solar wind irradiation[93] (high-energy ion implantation generates crystalline defects, making grains more susceptible to subsequent space weathering induced reshaping[94]; in addition, sputtering by solar wind may also erode particle surfaces[67]). Impact agglutination is distinctive in that it can transform "simple particles" into "complex particles" and operates cumulatively, producing highly irregular aggregates that strongly influence the overall particle morphology of the regolith. By contrast, other reshaping processes generally do not alter particle type (although "complex particles" may shed minor fragments of "simple particles"). Both "simple" and "complex" particles are subsequently modified by additional reshaping processes. Among these mechanisms, only impact gardening and impact fragmentation significantly modify regolith within a given depth, exerting the greatest influence on particle morphology. For impact fragmentation, previous studies have shown a correlation between the Is/FeO value, a surface exposure proxy, and mean particle size in regolith samples with particle sizes <1 cm (ref. 70); however, this correlation does not persist for mean particle sizes <1 mm. Moreover, Weibull statistics in rock mechanics model outputs demonstrate that smaller grains require higher stresses for complete failure[95,96]. Thus, for lunar regolith with mean grain sizes <1 mm, impact fragmentation likely contributes little to reshaping, with the deposited energy instead redistributed into broader-scale impact gardening. Consequently, impact gardening is considered the dominant driver of morphological modification in surface soils (Fig. 5). The bulk soil fraction of lunar regolith was the primary target of the micro-CT scans of this study, as it represents the dominant fraction. Despite notable differences in age, geological setting, lava origin, micrometeorite bombardment intensity, and solar wind irradiation between the CE5 and CE6 landing sites[24,25,31,54,97], the morphometrics of corresponding particle types remain remarkably consistent across both sites. This convergence indicates that long-term surface particle reshaping processes, dominated by impact gardening, have likely driven all particle types toward stable morphologies, such that further space weathering processes exert limited influence on particle morphometrics.

Moreover, the data imply that space weathering-induced morphological modification may have reached a saturation state within the bulk soil fraction of the youngest and least weathered CE5 regolith[46], with the onset of saturation thus occurring before ~2.2 Ma. To further test this potentially compelling hypothesis, we examined Apollo 17 sample 73002, collected from the upper ~20 cm of the Light Mantle landslide deposit at the base of the South Massif in the Taurus–Littrow Valley, a site at the mare-highland boundary characterized by a substantial proportion of highlands material and basalts of multiple ages[88,98]. The <1 mm fraction of this soil exhibits an Is/FeO value of ~74 (ref. 99) and a surface maximum exposure age of ~7.0 Ma (ref. 73), indicating a higher degree of space weathering than either CE5 or CE6 soils. To verify whether the same saturation trend holds for larger

https://doi.org/10.1038/s41467-026-68824-3

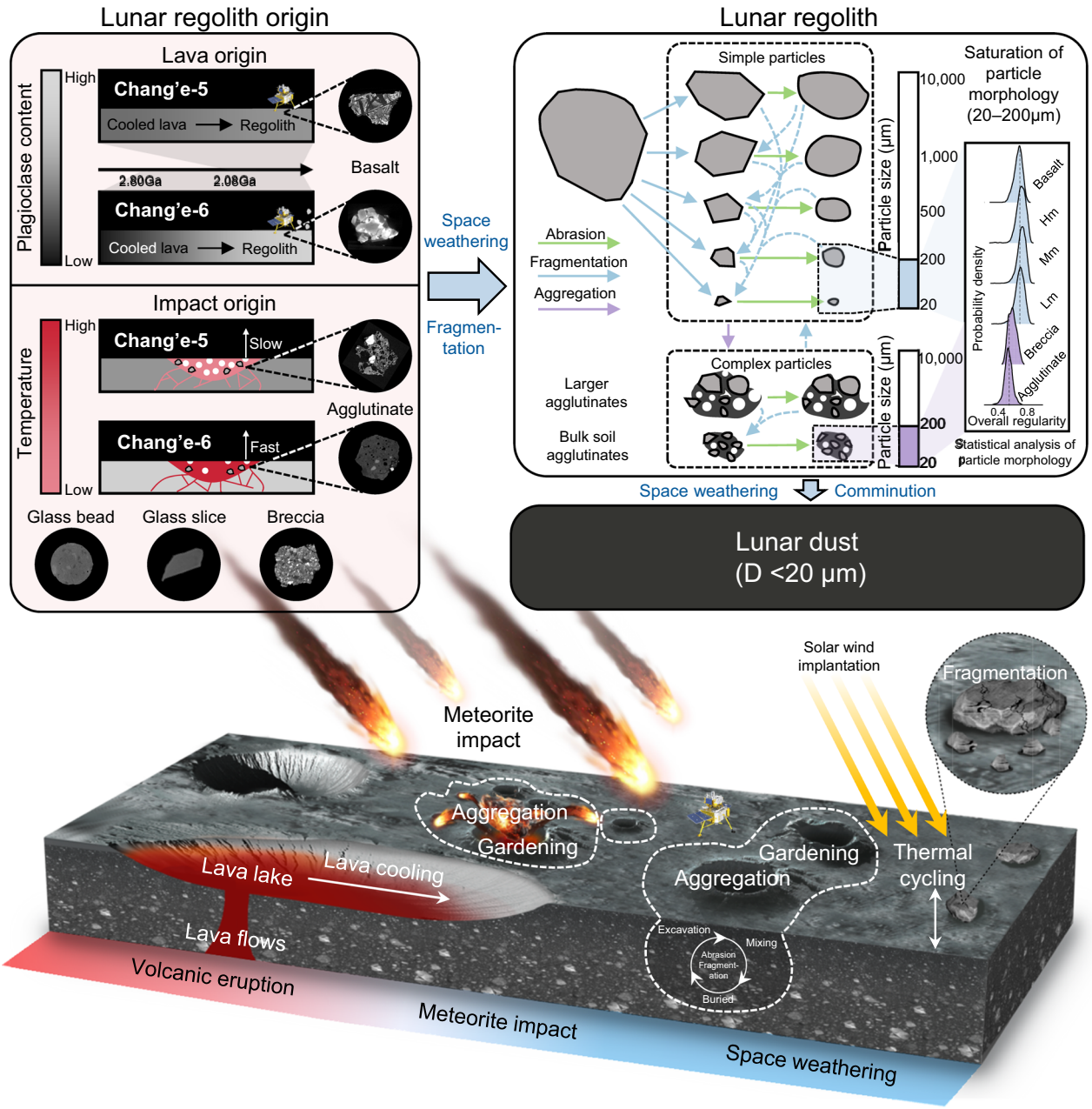

Fig. 5 | Tripartite geological–astronomical processes recorded by lunar regolith particles. Tripartite processes encoded in lunar regolith include (in progression): (i) volcanic eruption, (ii) meteorite impacting, and (iii) space weathering. In the CE5 region, the initial lava is characterized by a higher plagioclase content, whereas the CE6 regolith, over time, incorporated substantial amounts of exotic additional plagioclase-rich materials, resulting in a higher overall plagioclase abundance in the final regolith. Secondary products (including agglutinates, breccias, and glasses) are produced by meteorite impacts. Variations in impact intensity between the two landing sites likely contributed to the differing agglutinate void ratios observed. These disparities in internal structure and mineral composition collectively indicate that the CE5 and CE6 landing sites experienced distinct lava origins and impact histories. Following prolonged space weathering (maximum exposure age of >2.2 Ma), all types of particles in the bulk soil fraction exhibit saturation in morphological modification, as revealed here. Solid arrows indicate dominant processes with strong influence on particle morphology; dashed arrows represent weaker effects. As space weathering progresses, the fraction of lunar dust gradually increases until a steady-state grain size is reached.

particles, we focused on mare basalts. We selected 22 basalt particles (500–700 μm) from CE5, 27 particles of the same size range from CE6, and 110 particles from the upper 3 cm of Apollo 17 sample 73002 radiographs[88]. CE5 and CE6 basalts were analyzed using micro-CT scans at a voxel size of 25.8 μm, the same resolution as applied to the 73002 radiographs. Morphometric results show that the saturation state may persist even for larger particles in more strongly space-weathered soils, and even in 73002 regolith that is not pure mare material but instead contains more complex lithologic mixtures (Supplementary Fig. 9). However, further validation with larger datasets will nevertheless be required. During space weathering, regolith particles undergo repeated reshaping that ultimately leads to progressive soil comminution. Larger particles are continually broken down into the bulk soil fraction, while the bulk soil fraction itself steadily generates lunar dust. This process results in the gradual enrichment of lunar dust within the regolith (Fig. 5).

A comparison of morphometrics between lunar basalt particles and those produced by mechanical crushing of the LRS (Fig. 4a)

further suggests that abrasion driven by space weathering may act to increase aspect ratio while decreasing sphericity, convexity, and roundness. It is also noteworthy that agglutinates and breccia exhibit irregular morphology compared to other particle types (Fig. 4c), making them central to any accurate characterization of overall regolith morphology. Among commonly used morphological parameters, aspect ratio is frequently employed to describe the general geometry of both terrestrial and extraterrestrial particles[33,100]. However, while relatively insensitive to particle size effects, aspect ratio demonstrates limited discriminatory power for distinguishing agglutinates. In contrast, sphericity exhibits insensitivity to the scale effect but provides better deconvolution, with agglutinates consistently exhibiting lower sphericity than other particle types (Fig. 4b, c), rendering sphericity a more effective parameter for characterizing lunar regolith morphology in datasets where agglutinate content plays a major role.

Our study presents a saturation mode for regolith particle morphology. However, further verification of the model using more Apollo lunar samples or other micro-scale proxies, such as np-Fe^0 content and isotope analyses, is still needed. The observed saturation effect of space weathering in shaping the morphology of surficial lunar regolith particles, as revealed in the CE5 and CE6 samples, may well extend to other mare regions—with increasingly younger mare units potentially further refining the minimum saturation age. Also, once soil samples are retrieved from other airless terrestrial bodies, comparative analyses of particle morphometrics could offer insights into the relative dominance of space weathering processes (such as fragmentation versus abrasion) on those surfaces. For instance, surfaces experiencing more intense fragmentation may exhibit systematically lower aspect ratios, whereas the opposite result would suggest more abrasion. Building upon such a lunar-based model of regolith evolution, particle morphology could serve as a transferable diagnostic framework enabling the extension of this approach to characterize space weathering regimes on other planetary bodies, including other moons, planets, and asteroids.

Methods

Sample material and micro-CT scans

CE5 lunar sample (CE5C0400YJFM01001) and CE6 lunar sample (CE6C0200YJFM008) were allocated by the China National Space Administration (CNSA) for use in this study. These samples consisted of lunar soil containing various types of regolith particles. All samples were securely stored within a glove box, continuously purged with high-purity dry nitrogen gas (N_2 > 99.9999%, H_2O < 0.1 ppm, O_2 < 0.1 ppm) to prevent contamination and preserve sample integrity.

For micro-CT scans, ~200 mg of lunar soil was carefully transferred within the glove box into a transparent tube with an inner diameter of ~3 mm. After sealing the tube with a protective cap, the sample was removed from the glove box for micro-CT scans. X-ray tomography was performed using a Zeiss Xradia 620 Versa system at an accelerating voltage of approximately 60 kV, achieving a spatial resolution of 1 µm. Initially, a rapid overview scan was carried out at a lower resolution of 7.5 µm (~20 min per scan) to quickly assess the overall particle distribution within the bulk soil sample tube (Supplementary Fig. 1a). Subsequently, to optimize particle extraction efficiency from selected scan regions, six distinct scanning volumes were identified in both CE5 and CE6 samples, intentionally avoiding areas with large particles. Each detailed scan involved a full 360° rotation (~260 min per scan), producing ~1000 2D radiographs per region, covering a cylindrical volume of ~1 mm in diameter and 1 mm in height (Supplementary Video 3; Supplementary Video 4). This non-destructive approach was specifically chosen to maximize sample utilization while minimizing any potential alteration or damage.

A uniquely shaped subophitic-textured CE5 basalt particle and a CE6 breccia were specifically selected from a bulk soil CT scanning region to facilitate subsequent intensity-density calibration (Supplementary Fig. 2). The representative CE6 breccia particle was also used to verify segmentation accuracy of machine learning methods (Supplementary table. 1). After micro-CT scans, lunar samples were returned to the glove box and transferred into clean glass dishes. Representative basalt was manually isolated from the CE5 soil sample, whereas breccia was collected from the CE6 sample. To investigate the formation mechanism of lunar agglutinates, 42 relatively larger agglutinates (equivalent diameter >200 µm) were selected from the CE5 soil, and 42 from the CE6 soil. These 84 particles were mounted onto yellow transparent adhesive tape, and subsequently micro-CT rescanned individually at resolutions between 1.5 and 3.2 µm.

Radiograph intensity-density calibration

Radiograph intensities obtained from micro-CT scans reflect the degree of X-ray attenuation, influenced by multiple parameters such as X-ray energy and material density[101]. Intensity obtained from a radiograph can be quantitatively correlated with material density according to established relationships[23]. Prior to density calibration, pretreatment was performed on each set of radiographs using a non-local means filter for noise reduction and an unsharp masking filter for image sharpening via Avizo software (Supplementary Fig. 1a). As the X-ray attenuation characteristics remain stable under fixed scanning parameters, intensity normalization across all scanned regions of CE5 and CE6 bulk soil samples was achieved by standardizing intensity values from micro-CT radiographs to a uniform scale (0–255).

Two representative particles were utilized for the intensity–density calibration (Fig. 2a, Supplementary Fig. 2e, m). These selected particles were cut, and mineral phases within the polished thin section were identified using a Thermo Scientific Quattro S field-emission scanning electron microscope (SEM) equipped with a Thermo Scientific UltraDry energy dispersive X-ray spectroscopy (EDS) detector (Bruker XFlash6 | 30). The thin section was mounted directly onto conductive carbon adhesive tabs with either carbon foil or carbon-coated substrates. SEM imaging was conducted under optimized operational conditions: electron-beam accelerating voltages were set at 10–15 kV with electron beam currents ranging from 7–30 pA for high-resolution secondary electron imaging, whereas backscattered electron imaging and elemental mapping utilized voltages of 15–20 kV and beam currents of 50–120 pA.

Mineral distributions on thin sections were obtained (Supplementary Fig. 2e, m). Bulk soil CT scanning radiographs containing these two particles were spatially aligned to precisely match their corresponding SEM planes. Subsequently, four mineral phases of interest—plagioclase (Supplementary Fig. 2a, g), pyroxene (Supplementary Fig. 2b, h-l), olivine (Supplementary Fig. 2c) and ilmenite (Supplementary Fig. 2d)—were identified in the SEM images. Representative regions within each mineral phase were also selected for detailed elemental analyses using EDS, providing precise compositional data for atomic percent (Supplementary Table 2). Corresponding intensity values of these mineral regions were then extracted from aligned radiographs (Supplementary Fig. 2f, n). For density estimation, mineral densities were assigned based on literature values corresponding to mineral phases with elemental compositions closely matching those measured by EDS analysis[65] (Supplementary Table 2), enabling accurate linear calibration of the intensity–density relationship for the lunar samples (Supplementary Fig. 2o). It should be noted that although the coefficient of determination reaches 0.99, notable deviation arises in the intensity range >225, where the linear model becomes less valid due to X-ray attenuation effects in high-density materials[23]. Nevertheless, all polymineral particles and bulk soil averages presented in the density-related analyses (Supplementary Fig. 4) have mean intensities <150, within the valid linear range. Therefore, nonlinear effects were not considered in this study. Ilmenite, pyroxene or olivine, and plagioclase mineral phases correspond to Hp (intensity = 225–255), Mp (intensity =

130–225), and Lp (intensity = 64–130), respectively, allowing the construction of mineral phase distribution maps based on radiograph intensity (Supplementary Fig. 2f, n).

Segmentation

For radiographs with a resolution of 1 μm, particles with equivalent diameters >20 μm (effective particles) are sufficiently resolved to preserve relatively accurate 3D morphology and internal structures without significant distortion[102]. However, small particles and lunar dust complicate boundary identification due to insufficient resolution, making conventional threshold-based segmentation methods ineffective. To address this limitation, particle boundary extraction was performed using pixel classification-based machine learning via the open-source software ilastik[103]. Specifically, pixel classification was trained on 200 radiographs to robustly delineate particle boundaries, including internal pores and fractures, as well as to clearly differentiate effective particles from surrounding lunar dust and small particles (Supplementary Fig. 1b, d).

Due to the heterogeneous particle size distribution of lunar soils, extracting individual 3D particle shapes required additional segmentation. Traditional Chamfer-Conservative segmentation methods based on uniform boundary parameters proved ineffective for lunar soil because larger particles were prone to over-segmentation, whereas smaller particles frequently remained under-segmented[104]. To address this issue, a two-step "over-segmentation correction method" was implemented. Initially, an aggressive segmentation (Skeleton-Aggressive method) was conducted, capable of adequately separating smaller particles but inevitably causing over-segmentation of larger particles. Subsequently, segmentation lines were extracted and analyzed using Avizo. Segmentation lines representing accurately segmented smaller particles typically appeared spatially discrete (Supplementary Fig. 1b), whereas lines resulting from over-segmentation of large particles were interconnected. Therefore, to correct over-segmentation, lines corresponding to excessively segmented regions were identified and removed based on a threshold volume criterion. This filtering approach effectively retained accurate segmentation lines while eliminating erroneous segmentation lines. Following segmentation, effective particles for subsequent classification and morphological analysis. Particles smaller than 20 μm in equivalent diameter were retained solely for the purpose of quantifying the overall particle size distribution of the sample. The derived results show close agreement with bulk soil fraction contents independently obtained from extensive 2D imaging analyses of CE5 and CE6 soils[24,25] (Supplementary Fig. 11).

To quantitatively evaluate the accuracy of this segmentation procedure, a representative breccia particle from the CE6 lunar soil was physically isolated, rescanned individually, and compared to the same particle previously auto-segmented within the bulk soil CT scanning. The comparison demonstrated that key 3D morphological parameters, including particle volume and surface area, differed by less than 6% between bulk soil auto segmentation and direct measurements obtained from separate micro-CT scans of the manually selected particle (Supplementary Table 1).

Classification

Lunar regolith particles were initially categorized according to their mineralogical and textural features. Single-phase or homogeneous particles were classified based on intensity into three mineral-density groups: high-density (Hm, density > 4.72 g·cm^{-3}), intermediate-density (Mm, density= 3.21–4.72 g·cm^{-3}), and low-density (Lm, density <3.21 g·cm^{-3}) monomineralic particles. Polymineral particles exhibiting heterogeneous internal textures were classified into basalt, breccia, and agglutinate based on characteristic textural patterns observed internally[24,25].

Particle classification was conducted using the object classification module implemented in ilastik. A training dataset was manually generated by labeling particle types on 400 radiographs (200 images from the CE5 sample and 200 images from the CE6 sample), which were simultaneously trained to ensure consistent classification criteria across both lunar soils (Supplementary Fig. 1d). Subsequently, automated classification was performed, yielding preliminary particle-type classifications for every particles in each 2D slice. However, due to limited resolution, some small polymineral particles were challenging to classify accurately based solely on internal textures and were thus categorized as "unknown". It should be noted that many breccia particles, which are internally composed of fine fragments, could only be identified in this study when they were relatively large, contributing substantially to the total breccia volume (Fig. 4e) but representing a minor fraction in terms of particle count. At the bulk soil fraction, breccias were often broken down into monomineralic or polymineral debris, and due to resolution limitations, the internal clastic structure of smaller breccia particles was often indistinguishable. As a result, a significant number of small breccia particles may have been classified as "unknown". This category predominantly comprises polymineral particles and may also include small basalt and agglutinate fragments that could not be reliably identified. Based on these classification criteria, particles were categorized into seven types: basalt, agglutinate, breccia, Hm, Mm, Lm, and unknown.

Given the inherent textural heterogeneity within particles, inconsistent classifications across different slices within an individual 3D particle frequently occurred. To reconcile such inconsistencies arising from slice-by-slice classifications, a dedicated Python-based algorithm was developed to determine the statistically dominant particle type for each particle in 3D space (Supplementary Fig. 1c). Specifically, particle classification consistency was resolved based on "majority voting" strategy from 2D slice classifications, where each particle's final 3D category was assigned according to the following criterion:

$$kj = \max(ki) \tag{1}$$

where ki represents the total number of 2D slices within a given particle classified as particle type i (i = 1,2,3,4,5,6,7), and j represents the final 3D classification category assigned to the particle. Following classification, morphological parameters were analyzed for each particle, and particles with S > 0.92 were classified as glass beads.

Morphological parameters

Most morphological parameters analyzed in this study were dimensionless quantities commonly used in image analysis to characterize particle morphology independently of particle size. Particle size was quantified using the equivalent diameter D, defined as the diameter of a sphere having the same volume as the particle (Supplementary Fig. 10b)[105]:

$$\mathrm{D} = \sqrt[3]{\frac{6V}{\pi}} \tag{2}$$

where V represents the volume of the particle.

Axial ratios describe the proportional relationships among the three principal orthogonal dimensions, defined as P_1, P_2, and P_3 ($P_1 \geq P_2 \geq P_3$) (Supplementary Fig. 10a). The elongation index (EI), flatness index (FI), and aspect ratio (AR) were employed to quantify particle elongation and flatness, and are mathematically expressed as follows[106]:

$$\mathrm{EI} = \mathrm{P}_2/\mathrm{P}_1 \tag{3}$$

$$\mathrm{FI} = \mathrm{P}_3/\mathrm{P}_2 \tag{4}$$

$$AR = (\mathrm{EI} + \mathrm{FI})/2 \tag{5}$$

Sphericity (S) was defined as the ratio between the surface area of an equivalent-volume sphere (Supplementary Fig. 10b) and the actual particle surface area (SA), quantifying the closeness of particle shape to a perfect sphere[105]:

$$S = \frac{\sqrt[3]{36\pi V^2}}{SA} \tag{6}$$

Convexity (Cx) quantified the degree to which the particle shape resembles its corresponding convex hull and was defined as the ratio between the particle volume (V) and the volume of its convex hull (V_{ch}) (Supplementary Fig. 10c)[33,105]:

$$Cx = V/V_{ch} \tag{7}$$

Roundness (R) describes the relative curvature of a particle's projected outline. Specifically, it quantifies the sharpness of particle edges and corners and is calculated based on the particle's triangulated surface mesh projection[107,108]. The definition of roundness is the ratio of the average curvature of the corners of the particle to the curvature of the maximum inscribed circle (Supplementary Fig. 10 d)[33].

$$R = \frac{\sum_{i=1}^{N}(A_i k_i/k_m)}{\sum_{i=1}^{N}(A_i)} \tag{8}$$

where A_i is the area of the i-th triangular element, which is part of the corners on the particle, and k_i is the mean curvature of the i-th triangular element, and k_m is the curvature of the maximum inscribed sphere.

Overall regularity (OR), provides a composite description of the aforementioned morphological parameters and is defined as follows:

$$OR = (AR + S + Cx + R)/4 \tag{9}$$

Data availability

All data supporting this study are presented in the paper and its Supplementary Information. Source data are also provided with this paper. Source data are provided with this paper.

Code availability

All code used in this study is cited and no proprietary code was developed for this work.

References

1. Slyuta, E. N. Physical and mechanical properties of the lunar soil (a review). *Sol. Syst. Res.* **48**, 330–353 (2014).
2. O'Brien, P. & Byrne, S. Physical and Chemical Evolution of Lunar Mare Regolith. *JGR Planets* **126**, e2020JE006634 (2021).
3. Qian, Y. et al. Mineralogy and chronology of the young mare volcanism in the Procellarum-KREEP-Terrane. *Nat. Astron.* **7**, 287–297 (2023).
4. Zhang, H. et al. Size, morphology, and composition of lunar samples returned by Chang'E-5 mission. *Sci. China Phys. Mech. Astron.* **65**, 229511 (2022).
5. Apollo 16 Preliminary Examination Team. The Apollo 16 Lunar Samples: Petrographic and Chemical Description. *Science* **179**, 23–34 (1973).
6. Li, Q.-L. et al. Two-billion-year-old volcanism on the Moon from Chang'e-5 basalts. *Nature* **600**, 54–58 (2021).
7. Qian, Y., Xiao, L., Head, J. W. & Wilson, L. The Long Sinuous Rille System in Northern Oceanus Procellarum and Its Relation to the Chang'e-5 Returned Samples. *Geophys Res. Lett.* **48**, e2021GL092663 (2021).
8. He, Q. et al. Detailed petrogenesis of the unsampled Oceanus Procellarum: The case of the Chang'e-5 mare basalts. *Icarus* **383**, 115082 (2022).
9. Zhang, D. et al. Titanium in olivine reveals low-Ti origin of the Chang'E-5 lunar basalts. *Lithos* **414–415**, 106639 (2022).
10. Luo, B. et al. The magmatic architecture and evolution of the Chang'e-5 lunar basalts. *Nat. Geosci.* **16**, 301–308 (2023).
11. Head, J. W. & Wilson, L. Rethinking Lunar Mare Basalt Regolith Formation: New Concepts of Lava Flow Protolith and Evolution of Regolith Thickness and Internal Structure. *Geophys Res. Lett.* **47**, e2020GL088334 (2020).
12. Taylor, L. A., Pieters, C. M., Keller, L. P., Morris, R. V. & McKay, D. S. Lunar Mare Soils: Space weathering and the major effects of surface-correlated nanophase Fe. *J. Geophys. Res.* **106**, 27985–27999 (2001).
13. Sasaki, S., Nakamura, K., Hamabe, Y., Kurahashi, E. & Hiroi, T. Production of iron nanoparticles by laser irradiation in a simulation of lunar-like space weathering. *Nature* **410**, 555–557 (2001).
14. Noguchi, T. et al. Incipient Space Weathering Observed on the Surface of Itokawa Dust Particles. *Science* **333**, 1121–1125 (2011).
15. Hörz, F., Cintala, M. J., See, T. H., Cardenas, F. & Thompson, T. D. Grain size evolution and fractionation trends in an experimental regolith. *J. Geophys. Res. Solid Earth* **89**, C183–C196 (1984).
16. Devine, J. M., McKay, D. S. & Papike, J. J. Lunar Regolith: Petrology of the <10 μm fraction. *J. Geophys. Res.* **87**, (1982).
17. Li, L. et al. Transport of Volatiles in Agglutinates from Lunar Regolith of Chang'e-5 Mission. *Research* **8**, 0638 (2025).
18. Kling, A. M. et al. Nanoscale reservoirs store solar wind-derived water on the lunar surface. *Earth Planet. Sci. Lett.* **651**, 119178 (2025).
19. Wentworth, S. J., Keller, L. P., McKAY, D. S. & Morris, R. V. Space weathering on the Moon: Patina on Apollo 17 samples 75075 and 76015. *Meteorit. Planet. Sci.* **34**, 593–603 (1999).
20. Hörz, F., Basilevsky, A. T., Head, J. W. & Cintala, M. J. Erosion of lunar surface rocks by impact processes: a synthesis. *Planet. Space Sci.* **194**, 105105 (2020).
21. Weber, I. et al. Space weathering by simulated micrometeorite bombardment on natural olivine and pyroxene: A coordinated IR and TEM study. *Earth Planet. Sci. Lett.* **530**, 115884 (2020).
22. McKay D. S., Fruland R. M. & Heiken G. H. Grain size and the evolution of lunar soils. *Proc. 5th Lunar Sci. Conf.*, 887–906 (1974).
23. Wu, H. et al. Micro-CT Characterization of the Chang'e-5 Lunar Regolith Samples. *JGR Planets* **130**, e2024JE008787 (2025).
24. Li, C. et al. Nature of the lunar far-side samples returned by the Chang'E-6 mission. *Natl. Sci. Rev.* **11**, nwae328 (2024).
25. Li, C. et al. Characteristics of the lunar samples returned by the Chang'E-5 mission. *Natl. Sci. Rev.* **9**, nwab188 (2022).
26. Luo, A., Cui, Y., Nie, J. & Wang, G. Effects of adhesion and particle shape on mechanical behaviors of lunar regolith under low stress condition-3D DEM study. *Comput. Geotech.* **175**, 106661 (2024).
27. Ding, L. et al. Lunar rock investigation and tri-aspect characterization of lunar farside regolith by a digital twin. *Nat. Commun.* **15**, 2098 (2024).
28. Wu, F. Y. et al. Lunar evolution in light of the Chang'e-5 returned samples. *Annu. Rev. Earth Planet. Sci.* **52**, (2024).
29. Zhang, Q. W. L. et al. Lunar farside volcanism 2.8 billion years ago from Chang'e-6 basalts. *Nature* https://doi.org/10.1038/s41586-024-08382-0.(2024)
30. Tian, H.-C. et al. Non-KREEP origin for Chang'e-5 basalts in the Procellarum KREEP Terrane. *Nature* **600**, 59–63 (2021).
31. Yin, C. et al. Petrogenesis of Chang'e-6 Basalts and Implication for the Young Volcanism on the Lunar Faside. *ApJL* **981**, L2 (2025).

32. Zhang, H. Y. et al. Space weathering on the lunar nearside and farside constrained from Si isotopes. *Nat. Commun.* **16**, 1–7 (2025).
33. Nie, J. et al. Predicting residual friction angle of lunar regolith based on Chang'e-5 lunar samples. *Sci. Bull.* **68**, 730–739 (2023).
34. Matsushima, T. et al. 3D particle characteristics of highland lunar soil (No. 60501) obtained by micro X-ray CT. In *Earth & Space 2008: Engineering, Science, Construction, and Operations in Challenging Environments*, 1–8 (2008).
35. Katagiri, J. et al. Investigation of 3D Grain Shape Characteristics of Lunar Soil Retrieved in Apollo 16 Using Image-Based Discrete-Element Modeling. *J. Aerosp. Eng.* **28**, 04014092 (2015).
36. Chiaramonti, A. N., Goguen, J. D. & Garboczi, E. J. Quantifying the 3-Dimensional Shape of Lunar Regolith Particles Using X-Ray Computed Tomography and Scanning Electron Microscopy at Sub-γ Resolution. *Microsc Microanal.* **23**, 2194–2195 (2017).
37. Wilkerson, R. P., Rickman, D. L., McElderry, J. R., Walker, S. R. & Cannon, K. M. On the measurement of shape: With applications to lunar regolith. *Icarus* **412**, 115963 (2024).
38. Nie, J. Y., Cao, Z. J., Li, D. Q. & Cui, Y. F. 3D DEM insights into the effect of particle overall regularity on macro and micro mechanical behaviours of dense sands. *Comput. Geotech.* **132**, 103965 (2021).
39. Zhou, S. et al. Three-dimensional morphological analysis of Chang'e-5 lunar soil using deep learning-automated segmentation on computed tomography scans. *Computer-aided Civil Eng mice*.13487 https://doi.org/10.1111/mice.13487.(2025)
40. Li, L. & Li, J. Multimodal Particle Size Estimation of Lunar Soil Simulants Towards a Non-destructive Analytical Strategy for Extraterrestrial Samples. *Spectrosc.* **45**, 246–258 (2024).
41. Sakatani, N. et al. Anomalously porous boulders on (162173) Ryugu as primordial materials from its parent body. *Nat. Astron.* **5**, 766–774 (2021).
42. Cheng, B. et al. Reconstructing the formation history of top-shaped asteroids from the surface boulder distribution. *Nat. Astron.* **5**, 134–138 (2020).
43. Tatsumi, E. et al. Collisional history of Ryugu's parent body from bright surface boulders. *Nat. Astron.* **5**, 39–45 (2020).
44. Taylor, L. A. et al. The effects of space weathering on Apollo 17 mare soils: Petrographic and chemical characterization. *Meteorit. Planet. Sci.* **36**, 285–299 (2001).
45. Denevi, B. W. et al. Space weathering at the Moon. *Rev. Mineral. Geochem.* **89**, 1–56 (2023).
46. Cao, Z. et al. Nature of space-weathered rims on Chang'e-5 lunar soil grains. *Earth Planet. Sci. Lett.* **658**, 119327 (2025).
47. Keller, L. P. & McKay, D. S. The nature and origin of rims on lunar soil grains. *Geochim. Cosmochim. Acta* **61**, 2331–2341 (1997).
48. Noble S. K., Keller L. P., Christoffersen R. & Rahman Z. The microstructure of lunar micrometeorite impact craters. NASA Technical Report JSC-CN-35097 (2016).
49. Papike, J. J., Simon, S. B. & Laul, J. C. The lunar regolith: Chemistry, mineralogy, and petrology. *Rev. Geophys.* **20**, 761–826 (1982).
50. Adams, J. B., Charette, M. P. & Rhodes, J. M. Chemical fractionation of the lunar regolith by impact melting. *Science* **190**, 380–381 (1975).
51. Rhodes, J. M. et al. Chemistry of agglutinate fractions in lunar soils. *Proc. Lunar Sci. Conf.* **6**, 2291–2307 (1975).
52. Varatharajan, I., Srivastava, N. & Murty, S. V. Mineralogy of young lunar mare basalts: Assessment of temporal and spatial heterogeneity using M3 data from Chandrayaan-1. *Icarus* **236**, 56–71 (2014).
53. Boschi, S. et al. Compositional Variability of 2.0-Ga Lunar Basalts at the Chang'e-5 Landing Site. *JGR Planets* **128**, e2022JE007627 (2023).
54. Che, X. et al. Isotopic and compositional constraints on the source of basalt collected from the lunar farside. *Science* **387**, 1306–1310 (2025).
55. Neal, C. R. & Taylor, L. A. Petrogenesis of mare basalts: A record of lunar volcanism. *Geochim. Cosmochim. Acta* **56**, 2177–2211 (1992).
56. Wang, C. et al. A shallow (<100 km) ilmenite-bearing pyroxenitic source for young lunar volcanism. *Earth Planet. Sci. Lett.* **639**, 118770 (2024).
57. McKay, D. S. et al. The lunar regolith. *Lunar Sourceb.* **567**, 285–356 (1991).
58. Wang, K., Moynier, F., Podosek, F. A. & Foriel, J. An iron isotope perspective on the origin of the nanophase metallic iron in lunar regolith. *Earth Planet. Sci. Lett.* **337**, 17–24 (2012).
59. Xiong, M. et al. The formation mechanisms of np-Fe in lunar regolith: a review. *Materials* **17**, 5866 (2024).
60. Li, C. et al. Impact-driven disproportionation origin of nanophase iron particles in Chang'e-5 lunar soil sample. *Nat. Astron.* **6**, 1156–1162 (2022).
61. Shen, L. et al. Separate effects of irradiation and impacts on lunar metallic iron formation observed in Chang'e-5 samples. *Nat. Astron.* **8**, 1110–1118 (2024).
62. Huang, T. J., Ganju, E., Torbatisarraf, H., Thompson, M. S. & Chawla, N. Advanced microstructural and compositional analysis of a lunar agglutinate from the Apollo 11 mission. *Meteorit. Planet. Sci.* **59**, 1455–1472 (2024).
63. McKay D. S. & Ming DW. Properties of lunar regolith. In *Developments in Soil Science* **19**, 449–462 (Elsevier, 1990).
64. Via, W. N. & Taylor, L. A. Chemical aspects of agglutinate formation—relationships between agglutinate composition and the composition of the bulk soil. In *Proc. 7th Lunar Sci. Conf.* **7**, 393–403 (Pergamon Press, (1976).
65. Robie, R. A., Hemingway, B. S. & Fisher, J. R. *Thermodynamic Properties of Minerals and Related Substances at 298.15 K and 1 bar (10^5 pascals) Pressure and at Higher Temperatures*. U.S. Geol. Surv. Bull. 1452 (1978).
66. Ruan, R. et al. A moderate-Ti lunar mare soil simulant: IGG-01. *Acta Astronaut.* **224**, 148–160 (2024).
67. Tsuchiyama, A. et al. Three-dimensional shape distribution of lunar regolith particles collected by the Apollo and Luna programs. *Earth Planets Space* **74**, 172 (2022).
68. Tachibana, S. et al. Pebbles and sand on asteroid (162173) Ryugu: In situ observation and particles returned to Earth. *Science* **375**, 1011–1016 (2022).
69. McKay, D. S. & Basu, A. The production curve for agglutinates in planetary regoliths. *J. Geophys. Res. Solid Earth* **88**, B193–B199 (1983).
70. Morris, R. V. Surface exposure indices of lunar soils: A comparative FMR study. *Proc. 7th Lunar Sci. Conf.* **315**, 335 (1976).
71. Qian, Y. et al. First magnetic and spectroscopic constraints on attenuated space weathering at the Chang'e-5 landing site. *Icarus* **410**, 115892 (2024).
72. Li, J. et al. Magnetic signatures and origins of ferromagnetic minerals in Chang'e-6 lunar farside soils. *Nat. Commun.* **16**, 6218 (2025).
73. McFadden, J. A. et al. Analyzing the mineralogy and space weathering characteristics of the finest fraction in Apollo core sample 73002. *J. Geophys. Res. Planets* **129**, e2024JE008528 (2024).
74. Zhang, M., Fa, W. & Jia, B. Provenance and evolution of lunar regolith at the Chang'e-6 sampling site. *Nat. Astron.* **1**, 11 (2025).
75. Qian, Y. et al. China's Chang'e-5 landing site: Geology, stratigraphy, and provenance of materials. *Earth Planet. Sci. Lett.* **561**, 116855 (2021).

76. Xu, L. et al. Chronology, Local Stratigraphy, and Foreign Ejecta Materials at the Chang'e-6 Landing Site: Constraints on the Provenance of Samples Returned From the Moon's Farside. *Geophys Res. Lett.* **51**, e2024GL111311 (2024.
77. Nottingham, M. C. et al. Complex burial histories of Apollo 12 basaltic soil grains derived from cosmogenic noble gases: Implications for local regolith evolution and future in situ investigations. *Meteorit. Planet. Sci.* **57**, 603–634 (2022).
78. Guo, Z. et al. Nanophase Iron Particles Derived From Fayalitic Olivine Decomposition in Chang'E-5 Lunar Soil: Implications for Thermal Effects During Impacts. *Geophys Res. Lett.* **49**, e2021GL097323 (2022).
79. Wang, Z. et al. Chemical compositions of Chang'e-6 lunar soil and substantial addition of noritic crust ejecta from Apollo basin. *Geology* https://doi.org/10.1130/G53086.1 (2025).
80. Laul, J. C., Smith, M. R., Papike, J. J. & Simon, S. B. Agglutinates as recorders of regolith evolution: Application to the Apollo 17 drill core. *J. Geophys. Res.* **89**, (1984).
81. Cremonese, G., Borin, P., Lucchetti, A., Marzari, F. & Bruno, M. Micrometeoroids flux on the Moon. *Astron. Astrophys.* **551**, A27 (2013).
82. Jeong, M. et al. Multi-band polarimetry of the lunar surface. I. Global properties. *Astrophys. J. Suppl. Ser.* **221**, 16 (2015).
83. Harris, A. J. & Allen, J. S. I. I. I. One-, two-, and three-phase viscosity treatments for basaltic lava flows. *J. Geophys. Res. Solid Earth* **113**, B9 (2008).
84. Gonnermann H. M., Manga M. & Fagents S. A. Dynamics of magma ascent in the volcanic conduit. In *Modeling Volcanic Processes: The Physics and Mathematics of Volcanism* 55–84 (Cambridge Univ. Press, (2013).
85. Rust, A. C. & Cashman, K. V. Permeability of vesicular silicic magma: Inertial and hysteresis effects. *Earth Planet. Sci. Lett.* **228**, 93–107 (2004).
86. Nie, N. X., Dauphas, N., Zhang, Z. J., Hopp, T. & Sarantos, M. Lunar soil record of atmosphere loss over eons. *Sci. Adv.* **10**, eadm7074 (2024).
87. Li, C. et al. Impact-induced ultra-high melting point oldhamite discovered in Chang'E-6 lunar soil. *Nat. Commun.* **16**, 2155 (2025).
88. Eckley, S. A. et al. Utilization of X-ray computed tomography during the preliminary examination of unopened Apollo drive tube samples 73001 and 73002. *J. Geophys. Res. Planets* **130**, e2024JE008583 (2025).
89. Lin, H. et al. Higher water content observed in smaller size fraction of Chang'e-5 lunar regolith samples. *Sci. Bull.* **69**, 3723–3729 (2024).
90. Ruesch, O. et al. In situ fragmentation of lunar blocks and implications for impacts and solar-induced thermal stresses. *Icarus* **336**, 113431 (2020).
91. Harries, D. & Langenhorst, F. The mineralogy and space weathering of a regolith grain from 25143 Itokawa and the possibility of annealed solar wind damage. *Earth Planets Space* **66**, 163 (2014).
92. Yan, P. et al. Intricate regolith reworking processes revealed by microstructures on lunar impact glasses. *J. Geophys. Res. Planets* **127**, e2022JE007260 (2022).
93. Pieters, C. M. & Noble, S. K. Space weathering on airless bodies. *JGR Planets* **121**, 1865–1884 (2016).
94. Maurette, M. & Price, P. B. Electron microscopy of irradiation effects in space: Radiation-damaged lunar and meteoritic grains tell us about solar system history and synthesis of molecules in space. *Science* **187**, 121–129 (1975).
95. McDowell, G. R. & Amon, A. The application of Weibull statistics to the fracture of soil particles. *Soils Found.* **40**, 133–141 (2000).
96. Weibull, W. A statistical distribution function of wide applicability. *J. Appl. Mech.* **18**, 293–297 (1951).
97. Lin, J. et al. Differences in space weathering between the near and far side of the Moon: evidence from Chang'e-6 samples. *Natl. Sci. Rev.* **12**, nwaf087 (2025).
98. Neuman, M. et al. Revealing the Moon's Taurus–Littrow landslide via integrated analysis of pristine Apollo 17 soil core 73001/2. *J. Geophys. Res. Planets* **130**, e2024JE008556 (2025).
99. Morris, R. V. et al. Stratigraphy of the Apollo 17 landslide core 73002 from FMR maturity and VNIR and Mössbauer spectroscopy. *Lunar Planet. Sci. Conf.* (2022).
100. Deitrick, S. R. & Cannon, K. M. Characterizing detailed grain shape and size distribution properties of lunar regolith. In *53rd Lunar Planet. Sci. Conf.* abstr. #1183 (2022).
101. Sudhyadhom, A. On the molecular relationship between Hounsfield Unit (HU), mass density, and electron density in computed tomography (CT). *PLoS ONE* **15**, e0244861 (2020).
102. Zhao, B., Wang, J., Coop, M. R., Viggiani, G. & Jiang, M. An investigation of single sand particle fracture using X-ray micro-tomography. *Géotech.* **65**, 625–641 (2015).
103. Berg, S. et al. ilastik: interactive machine learning for (bio)image analysis. *Nat. Methods* **16**, 1226–1232 (2019).
104. Luo, X. et al. Pore structure characterization and seepage analysis of ionic rare earth orebodies based on computed tomography images. *Int. J. Min. Sci. Technol.* **32**, 411–421 (2022).
105. Li, L., Sun, Q. & Iskander, M. Efficacy of 3D dynamic image analysis for characterising the morphology of natural sands. *Géotech.* **73**, 586–599 (2023).
106. Robin, C. Q. et al. Mechanical properties of rubble pile asteroids (Dimorphos, Itokawa, Ryugu, and Bennu) through surface boulder morphological analysis. *Nat. Commun.* **15**, 6203 (2024).
107. Wadell, H. Volume, shape, and roundness of rock particles. *J. Geol.* **40**, 443–451 (1932).
108. Wadell, H. Sphericity and roundness of rock particles. *J. Geol.* **41**, 310–331 (1933).
109. Chen, J. et al. Digital and global lithologic mapping of the Moon at a 1:2,500,000 scale. *Sci. Bull.* **67**, 2050–2054 (2022).
110. Cone, K. A. ApolloBasalt DB_V2, version 1.0. *Interdisciplinary Earth Data Alliance (IEDA)* https://doi.org/10.26022/IEDA/111982 (2021).

Acknowledgements

This work was funded by the National Natural Science Foundation of China 42241109 (Y.F.C.) and 42577187 (J.Y.N.) and Tsinghua University Initiative Scientific Research Program 20253080040 (Y.F.C.). The financial support from the Young Elite Scientists Sponsorship Program by CAST 2023QNRC001 (J.Y.N.) is gratefully acknowledged. We would also like to appreciate the China National Space Administration for providing the invaluable lunar samples from both the Chang'e-5 and Chang'e-6 missions.

Author contributions

A.L., Y.F.C., G.D.W., J.Y.N., and Y.L. conceived and designed the experiments. A.L., G.D.W., J.Y.N., and C.S.X. performed the experiments. A.L., Y.F.C., G.D.W., J.Y.N., Z.H.Z., Q.Z., and H.Y.H analyzed the data. A.L., Y.F.C., G.D.W., and J.Z. contributed materials tools. A.L. and Y.F.C. wrote the paper.

Competing interests

The authors declare no competing interests.

Additional information

Supplementary information The online version contains supplementary material available at https://doi.org/10.1038/s41467-026-68824-3.

Correspondence and requests for materials should be addressed to Yifei Cui, Guodong Wang or Jiayan Nie.

Peer review information *Nature Communications* thanks Takashi Matsushima and the other anonymous reviewer for their contribution to the peer review of this work. A peer review file is available.